Hovering UAV-Based FSO Communications: Channel Modelling, Performance Analysis, and Parameter Optimization

Jin-Yuan Wang, *Member, IEEE*, Yang Ma, Rong-Rong Lu, Jun-Bo Wang, *Member, IEEE*, Min Lin, *Member, IEEE*, and Julian Cheng, *Senior Member, IEEE*

***Abstract*— Relay-assisted free-space optical (FSO) communication systems are exploited as a means to mitigate the limiting effects of the turbulence induced atmospheric scintillation. However, conventional ground relays are stationary, and their optimal placement is not always feasible. Due to their mobility and flexibility, unmanned aerial vehicles (UAVs) provide new opportunities for FSO relaying systems. In this paper, a hovering UAV-based serial FSO decode-and-forward relaying system is investigated. In the channel modelling for such a system, four types of impairments (i.e., atmospheric loss, atmospheric turbulence, pointing error, and link interruption due to angle-of-arrival fluctuation) are considered. Based on the proposed channel model, a tractable expression for the probability density function of the total channel gain is obtained. Closed-form expressions of the link outage probability and end-to-end outage probability are derived. Asymptotic outage performance bounds for each link and the overall system are also presented to reveal insights into the impacts of different impairments. To improve system performance, we optimize the beam width, field-of-view and UAVs' locations. Numerical results show that the derived theoretical expressions are accurate to evaluate the outage performance of the system. Moreover, the proposed optimization schemes are efficient and can improve performance significantly.**

***Index Terms*— FSO communications, outage probability, parameter optimization, relay, UAV.**

Manuscript received October 15, 2020; revised March 2, 2021; accepted April 12, 2021. Date of publication June 14, 2021; date of current version September 16, 2021. This work was supported in part by the Open Research Fund of Key Laboratory of Broadband Wireless Communication and Sensor Network Technology under Grant JZNY202115, in part by the Open Project of Shanghai Key Laboratory of Trustworthy Computing, in part by the Opening Foundation of Key Laboratory of Opto-Technology and Intelligent Control, Ministry of Education under Grant KFKT2020-06, in part by the National Key Research and Development Program under Grant 2018YFB1801905, in part by the National Natural Science Foundation of China under Grant 61960206005 and Grant 61960206006, in part by the Jiangsu Province Basic Research Project under Grant BK20192002, and in part by the Key International Cooperation Research Project under Grant 61720106003. This article was presented at the IEEE International Conference on Communications, Dublin, Ireland, 2020 [1]. *(Corresponding authors: Jin-Yuan Wang; Jun-Bo Wang.)*

Jin-Yuan Wang is with the Key Laboratory of Broadband Wireless Communication and Sensor Network Technology, Nanjing University of Posts and Telecommunications, Nanjing 210003, China, also with the Shanghai Key Laboratory of Trustworthy Computing, East China Normal University, Shanghai 200062, China, and also with the Key Laboratory of Opto-Technology and Intelligent Control, Lanzhou Jiaotong University, Lanzhou 730070, China (e-mail: jywang@njupt.edu.cn).

Yang Ma and Jun-Bo Wang are with the National Mobile Communications Research Laboratory, Southeast University, Nanjing 211111, China (e-mail: yangma@seu.edu.cn; jbwang@seu.edu.cn).

Rong-Rong Lu and Min Lin are with the College of Telecommunications and Information Engineering, Nanjing University of Posts and Telecommunications, Nanjing 210003, China (e-mail: 1019010205@njupt.edu.cn; linmin@njupt.edu.cn).

Julian Cheng is with the School of Engineering, The University of British Columbia, Kelowna, BC V1V 1V7, Canada (e-mail: julian.cheng@ubc.ca).

Color versions of one or more figures in this article are available at https://doi.org/10.1109/JSAC.2021.3088656.

Digital Object Identifier 10.1109/JSAC.2021.3088656

I. Introduction

RECENTLY, free-space optical (FSO) communications has attracted considerable attention to overcome the spectrum congestion problem [2], [3], because unlike the radio frequency (RF) wireless communications, FSO communications are unlicensed, directional, immune to electromagnetic interference, and not easily intercepted. Nevertheless, it is widely acknowledged that the terrestrial FSO signal is impaired by three important factors including atmospheric loss, atmospheric turbulence, and pointing error, which are all distance-dependent [4]. Moreover, the transceivers in FSO communications are limited by the strict requirement of line-of-sight (LoS) alignment [5]. These disadvantages lead to the development of the relay-assisted FSO communications [6], whereby relays are placed properly between the source and the destination to improve system performance and reliability. However, affected by the obstacles (such as lakes, mountains and buildings), the optimal positions to deploy relays may not be always feasible, and thus novel relaying schemes should be exploited.

To revolutionize the commonly-employed relaying network architectures, the unmanned aerial vehicle (UAV) based relaying scheme was proposed for FSO communications [7]. Compared with the conventional terrestrial relays, UAV-based relays have the intrinsic advantages of finding better communication environment and establishing the LoS links by adjusting positions dynamically. With the perfect combination of FSO communications and UAVs, the UAV-based FSO communication system is currently gaining significant attention, which is regarded as a promising technology in many fields, such as emergency response and military operation [8]–[10]. It is expected that employing UAVs in FSO communication systems will inspire promising and innovative applications for future communication systems.

For UAV-based FSO relaying systems, accurate channel modeling, tractable performance indicator expressions and

efficient parameters optimization methods are of vital importance. Several analytical models for hovering UAV based FSO communications were proposed [11]. In [12], the alignment and stability analyses for inter-UAV communications were presented. In [13], the ergodic sum rate for a UAV-based relay network with mixed RF/FSO channel was derived, and the joint effects of the atmospheric loss, the atmospheric turbulence, and the geometric and misalignment loss on the FSO channel were considered. In [14], the throughput for a UAV-based mixed FSO/RF system with a buffer constraint was analyzed. Note that the effects of the angle-of-arrival (AoA) fluctuations of due to orientation deviations of hovering UAVs were not considered in [11]–[14]. By considering the non-orthogonality of the laser beam and the random fluctuations of the UAV's orientation and position, a novel channel model was proposed for UAV-based FSO communications [15]. In [16], the FSO channel impaired by weak turbulence, pointing error and AoA fluctuation was established. By considering the AoA fluctuation and pointing error, the outage performance of an FSO communication system operating on high-altitude airborne platforms was investigated [17]. Recently, by jointly considering the effects of atmospheric attenuation, atmospheric turbulence, pointing error and link interruption due to AoA fluctuation, a novel statistical channel model for hovering UAV-based FSO communications was derived [18]. In [19], by taking into account the effect of nonzero boresight pointing error, an extended model is established for UAV-based FSO communications. However, due to the large number of complex functions and operators, the derived expressions [18], [19] are cumbersome, and intuitive insights cannot easily be obtained for system design. To facilitate the parameter optimization, we are motivated to develop tractable channel models and theoretical expressions.

For parameter optimizations, there exist two fundamental tradeoffs in UAV-based FSO communications [16], [17], [20], [21]. First, the beam width balances the fading of pointing error and the strength of received signal. That is, increasing beam width will mitigate the impact of pointing error, but it also reduces the strength of the received signal. Second, the selection of field-of-view (FoV) involves a tradeoff between AoA fluctuation and received noise. In other words, increasing the value of FoV can reduce the impact of AoA fluctuation but increase the received noise as well. For network optimizations, the deployment or trajectory of UAVs can be designed to take full advantage of their ultra-flexibilities. Such topics have been studied in open literature. In [22]–[24], the performance indicators like system throughput, network coverage, energy efficiency, and task completion time were optimized to find the optimal static locations or trajectory of UAVs. When designing the UAVs' trajectory, most prior solutions rely on simplified channel models that are based on either the assumption that LoS link always exists or the LoS statistic model. However, in reality, the LoS link may be obstructed by some obstacles (such as mountains and buildings). In other words, the LoS link may not always be available in practical systems. Therefore, the existence of the LoS link should be considered in the parameter optimization process [25]. Consequently, an important question arises: How to efficiently find LoS link and obtain satisfied system performance for UAV-based FSO communication systems with obstacles? Under the obstacle scenario, the UAV's location was optimized within a feasible region bounded by the minimum accepted elevation angles of source and destination [26]. Note that the AoA fluctuation in [26] is ignored, the considered log-normal distributed turbulence is only suitable for weak turbulence, and the feasible region limits the deployment of UAVs. Therefore, the parameter optimization problem in UAV-based FSO communications should be further investigated.

Motivated by the aforementioned discussions, this paper focuses on a hovering UAV-based serial relaying FSO communication system, and further investigates the channel modeling, performance analysis and parameter optimization problems. The contributions of this paper are summarized as follows:

- *Channel modeling*: The considered FSO system involves three kinds of links, i.e., the ground-to-UAV (GU) link, the UAV-to-UAV (UU) link, and the UAV-to-ground (UG) link. For each link, the effects of atmospheric loss, atmospheric turbulence, pointing error and link interruption due to AoA fluctuation are jointly considered. Different from [18], we consider the independence of four impairments, and obtain a simple and tractable expression for the probability density function (PDF) of the total channel gain, which can be effectively used for performance analysis. The accuracy of the derived PDF is verified in Section V.
- *Performance analysis*: Based on the derived PDF of the total channel gain, the closed-form expressions of the link outage probability and the end-to-end outage probability are derived. Through asymptotic analysis, the asymptotic bounds of the link outage probability and the end-to-end outage probability are then obtained. Furthermore, insights about the derived expressions are also provided. Numerical results verify the accuracy of the derived theoretical expressions, and these expressions can be directly utilized to evaluate system performance rapidly without time-intensive simulations.
- *Parameter optimization*: To further improve the system performance, the beam width, the FoV and the UAVs' locations are optimized. Specifically, the minimum beam width is derived first, and the actual beam width of each link should be adjusted to be larger than or equal to the minimum value. Then, the FoV is optimized by minimizing the end-to-end outage probability with the beam width constraint, and the asymptotically optimal FoV is derived by solving a nonlinear equation. Finally, under the obstacle scenario, the locations of UAVs are optimized by solving a minimization problem. Then, the problem is transformed to a min-max problem, which can be effectively solved by using the embedded function "fmincon" in MATLAB [25]. Numerical results verify the effectiveness of the proposed parameter optimization schemes.

The rest of the paper is organized as follows. Section II presents the system model. In Section III, the exact outage probabilities and the corresponding asymptotic bounds for the UAV-based FSO relaying system are analyzed. In Section IV,

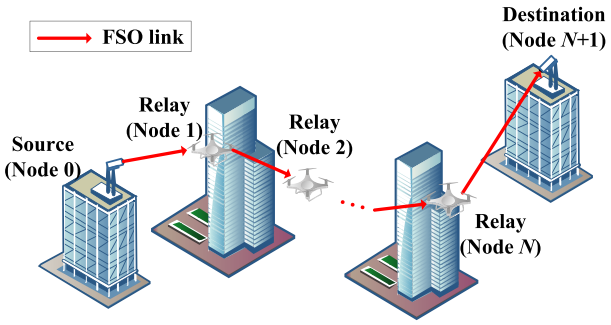

Fig. 1. A UAV-assisted serial relaying FSO communication systems.

the parameter optimization is further investigated. Numerical results are presented in Section V. Finally, Section VI concludes the paper.

Notations: Throughout this paper, regular font indicates a scalar. $X \sim \mathcal{N}(\mu, \sigma^2)$ denotes that X follows a Gaussian distribution having mean μ and variance σ^2; $\Gamma(\cdot)$ denotes the Gamma function; $K_n(\cdot)$ denotes the modified Bessel function of the second kind with order n [27]; $\mathrm{erf}(x) = \frac{2}{\sqrt{\pi}} \int_0^x e^{-t^2} \mathrm{d}t$ denotes the error function; $\delta(\cdot)$ denotes the Dirac delta function; $G_{p,q}^{m,n}[\cdot]$ is the Meijer's G-function [27]; and $\Pr(\cdot)$ denotes the probability of an event.

II. System Model

As shown in Fig. 1, we consider a UAV-based multi-hop relaying FSO communication system, which includes one source node, one destination node, and N UAV-based serial relay nodes. In the system, the transmit optical signal from the source node propagates through N serial relay nodes before detection at the destination node. Specifically, the source node is equipped with a laser diode (LD) and transmits the optical signal to the first relay node. For each relay node, a photodiode (PD) is first employed to convert the received optical signal to electrical signal, the decode-and-forward (DF) relaying scheme is then implemented, and the recovered signal is finally converted to optical signal by using an LD and transmitted to the next node. At the detection node, a PD is utilized to perform the photoelectric conversion. Different from the ground fixed relays, the relay nodes are assumed to be mounted on the UAVs. Moreover, we assume that the UAVs hover at their own fixed positions, and the orientations of the transceiver in each link are aligned with each other. However, the instantaneous positions of the relay nodes and the orientations of the transceiver deviate from the mean values due to numerous random events related to UAV hovering or building swaying.

A. Received Signal Model

Here, the intensity modulation and direct detection is employed and the on-off keying (OOK) is used as the modulation scheme. For simplification, the source node is denoted by node 0, the relay nodes are denoted by nodes $1, 2, \cdots, N$, and the destination node is denoted by node $N+1$. In the considered system, there are $N+1$ links, and the ith link is built by node $i-1$ and node i. Mathematically, the received electrical signal at node i in the ith link is given by

$$y_i = R h_i x_i + n_i, \quad i = 1, \cdots, N+1, \tag{1}$$

where R is the optoelectronic conversion factor of the PD at node i; x_i is the transmitted optical signal of node $i-1$; h_i is the channel gain of the ith link, and n_i is the signal-independent additive white Gaussian noise having mean zero and variance $\sigma_{\mathrm{n},i}^2$, i.e., $n_i \sim \mathcal{N}(0, \sigma_{\mathrm{n},i}^2)$. The transmitted optical signal is taken as symbols drawn equal-probably from the OOK constellation such that $x_i \in \{0, 2P_\mathrm{t}\}$, and P_t is the average transmitted optical power per link, which is related to the total transmit optical power P by $P_\mathrm{t} = P/(N+1)$. At each receiver, the background noise is assumed to be the dominant noise source, and the noise variance is a quadratic function with respect to the FoV of the receiver [18], i.e.,

$$\sigma_{\mathrm{n},i}^2 = \Lambda \theta_{\mathrm{FoV},i}^2, \tag{2}$$

where Λ is a coefficient related to the wavelength, bandwidth of the optical filter, spectral radiance and lens area. $\theta_{\mathrm{FoV},i}$ is the receiver's FoV at node i.

B. Channel Model

There are three types of links in the considered system, i.e., the GU link, the UU links, and the UG link. Actually, the first link is the GU link, the $(N+1)$th link is the UG link, and all other links (i.e., from the second link to the Nth link) belong to the UU links. For all the links, the total channel gain h_i can be formulated as a product of four impairments, i.e.,

$$h_i = h_i^{(\mathrm{l})} h_i^{(\mathrm{a})} h_i^{(\mathrm{pe})} h_i^{(\mathrm{aoa})}, \quad i = 1, \cdots, N+1, \tag{3}$$

where $h_i^{(\mathrm{l})}$ is the atmospheric loss, $h_i^{(\mathrm{a})}$ is the atmospheric turbulence, $h_i^{(\mathrm{pe})}$ is the pointing error, and $h_i^{(\mathrm{aoa})}$ is the link interruption due to AoA fluctuation. Inspired by the ideas in [17], [18] and [25], three typical adjustable parameters (i.e., beam width, FoV, and link distance) are considered to be different in each link for the sake of the system parameter optimization, and the other parameters are assumed to be the same in all $N+1$ links unless otherwise stated. In the following, the statistical characteristic of the four impairments will be analyzed, respectively.

1) Atmospheric Loss: Referring to [28], the atmospheric loss $h_i^{(\mathrm{l})}$ is determined by the exponential Beers-Lambert law as

$$h_i^{(\mathrm{l})} = \exp(-Z_i \Phi), \quad i = 1, \cdots, N+1, \tag{4}$$

where Z_i is the distance of the ith link, and Φ is the atmospheric attenuation coefficient related to visibility.

2) Atmospheric Turbulence: For the atmospheric turbulence, the Gamma-Gamma fading model is used here since its distribution is in close agreement with measurements under various turbulence conditions. Therefore, the PDF of $h_i^{(\mathrm{a})}$ is given by [29]

$$f_{h_i^{(\mathrm{a})}}\left(h_i^{(\mathrm{a})}\right) = \frac{2(\alpha_i \beta_i)^{\frac{\alpha_i+\beta_i}{2}}}{\Gamma(\alpha_i)\Gamma(\beta_i)} (h_i^{(\mathrm{a})})^{\frac{\alpha_i+\beta_i}{2}-1} \times K_{\alpha_i-\beta_i}\left(2\sqrt{\alpha_i \beta_i h_i^{(\mathrm{a})}}\right), \quad i = 1, \cdots, N+1, \tag{5}$$

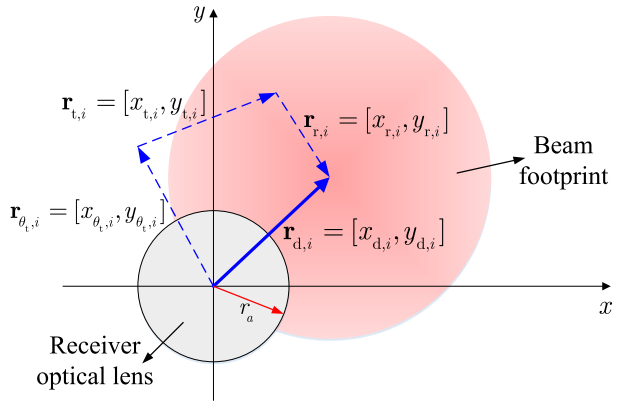

Fig. 2. The Gaussian beam footprint at receiver aperture for the ith link.

where the parameters α_i and β_i related to large-scale and small-scale eddies are given by

$$\begin{cases} \alpha_i = \left[\exp\left(\dfrac{0.49\sigma_{\mathrm{R},i}^2}{\left(1+1.11\sigma_{\mathrm{R},i}^{12/5}\right)^{7/6}} \right) - 1 \right]^{-1} \\ \beta_i = \left[\exp\left(\dfrac{0.51\sigma_{\mathrm{R},i}^2}{\left(1+0.69\sigma_{\mathrm{R},i}^{12/5}\right)^{5/6}} \right) - 1 \right]^{-1}, \end{cases} \tag{6}$$

where $\sigma_{\mathrm{R},i}^2 = 1.23 C_n^2 k^{7/6} Z_i^{11/6}$ is the Rytov variance related to the link distance Z_i, C_n^2 is the index of refraction structure parameter of atmosphere, and $k = 2\pi/\lambda$ is the optical wave number with λ being the wavelength.

3) Pointing Error: Fig. 2 shows the Gaussian beam footprint at receiver aperture, where the beam is orthogonal to the receiver lens plane. We consider a circular detection aperture of radius r_a at node i, $i = 1, \cdots, N+1$. The radial displacement vector from the receiving aperture center to the beam center is expressed as $\mathbf{r}_{\mathrm{d},i} = [x_{\mathrm{d},i}, y_{\mathrm{d},i}]$, which results from three different vectors: i) the displacement vector induced by the transmitter's orientation deviation $\mathbf{r}_{\theta_{\mathrm{t}},i} = [x_{\theta_{\mathrm{t}},i}, y_{\theta_{\mathrm{t}},i}]$, ii) the displacement vector induced by the transmitter's position deviation $\mathbf{r}_{\mathrm{t},i} = [x_{\mathrm{t},i}, y_{\mathrm{t},i}]$, and iii) the displacement vector induced by the receiver's position deviation $\mathbf{r}_{\mathrm{r},i} = [x_{\mathrm{r},i}, y_{\mathrm{r},i}]$. Consequently, the displacements located along the horizontal axe and the vertical axe at the detector plane are, respectively, given by

$$\begin{cases} x_{\mathrm{d},i} = x_{\mathrm{t},i} + x_{\mathrm{r},i} + x_{\theta_{\mathrm{t}},i} \\ y_{\mathrm{d},i} = y_{\mathrm{t},i} + y_{\mathrm{r},i} + y_{\theta_{\mathrm{t}},i}. \end{cases} \tag{7}$$

According to the central limit theorem, the position and orientation deviations follow Gaussian distributions as they result from numerous random events [18].

a) UU links: For these links, both $x_{\mathrm{t},i}$ and $x_{\mathrm{r},i}$ follow the same Gaussian distribution with mean zero and variance $\sigma_{\mathrm{p,u}}^2$, i.e., $x_{\mathrm{t},i}, x_{\mathrm{r},i} \sim \mathcal{N}(0, \sigma_{\mathrm{p,u}}^2)$. Moreover, $x_{\theta_{\mathrm{t}},i} = Z_i \tan\theta_{\mathrm{tx},i} \simeq Z_i \theta_{\mathrm{tx},i}$, where $\theta_{\mathrm{tx},i} \sim \mathcal{N}(0, \sigma_{\mathrm{angle,u}}^2)$. This indicates that $x_{\theta_{\mathrm{t}},i} \sim \mathcal{N}(0, Z_i^2 \sigma_{\mathrm{angle,u}}^2)$. Similarly, the distribution of $y_{\mathrm{d},i}$ can also be analyzed. As a result, $x_{\mathrm{d},i}, y_{\mathrm{d},i} \sim \mathcal{N}(0, 2\sigma_{\mathrm{p,u}}^2 + Z_i^2 \sigma_{\mathrm{angle,u}}^2)$.

b) GU link: For the first link, $\theta_{\mathrm{tx},1}$ is zero. The variances of position deviation $x_{\mathrm{t},1}$ is assumed to be zero-mean Gaussian distribution with variance $\sigma_{\mathrm{p,g}}^2$, i.e., $x_{\mathrm{t},1} \sim \mathcal{N}(0, \sigma_{\mathrm{p,g}}^2)$. Moreover, we can obtain $x_{\mathrm{r},1} \sim \mathcal{N}(0, \sigma_{\mathrm{p,u}}^2)$. Therefore, $x_{\mathrm{d},1}, y_{\mathrm{d},1} \sim \mathcal{N}(0, \sigma_{\mathrm{p,u}}^2 + \sigma_{\mathrm{p,g}}^2)$.

c) UG link: Referring to the analysis for GU and UU links, we can obtain $x_{\mathrm{t},N+1} \sim \mathcal{N}(0, \sigma_{\mathrm{p,g}}^2)$, $x_{\mathrm{r},N+1} \sim \mathcal{N}(0, \sigma_{\mathrm{p,u}}^2)$, and $x_{\theta_{\mathrm{t}},N+1} \sim \mathcal{N}(0, Z_{N+1}^2 \sigma_{\mathrm{angle,u}}^2)$ for the $(N+1)$th link. Consequently, $x_{\mathrm{d},N+1}, y_{\mathrm{d},N+1} \sim \mathcal{N}(0, \sigma_{\mathrm{p,u}}^2 + \sigma_{\mathrm{p,g}}^2 + Z_{N+1}^2 \sigma_{\mathrm{angle,u}}^2)$.

Assuming that the variables in (7) are independent of each other [18], the total radial displacement can be expressed as $r_{\mathrm{tr},i} = \sqrt{x_{\mathrm{d},i}^2 + y_{\mathrm{d},i}^2}$, which follows a Rayleigh distribution, i.e.,

$$f_{r_{\mathrm{tr},i}}(r_{\mathrm{tr},i}) = \frac{r_{\mathrm{tr},i}}{\sigma_{\mathrm{s},i}^2} \exp\left(-\frac{r_{\mathrm{tr},i}^2}{2\sigma_{\mathrm{s},i}^2} \right), \quad r_{\mathrm{tr},i} \geq 0, \tag{8}$$

where the total displacement variances $\sigma_{\mathrm{s},i}^2$ for different links are derived as

$$\sigma_{\mathrm{s},i}^2 = \begin{cases} \sigma_{\mathrm{p,u}}^2 + \sigma_{\mathrm{p,g}}^2, & i = 1 \\ 2\sigma_{\mathrm{p,u}}^2 + Z_i^2 \sigma_{\mathrm{angle,u}}^2, & i = 2, \ldots, N \\ \sigma_{\mathrm{p,u}}^2 + \sigma_{\mathrm{p,g}}^2 + Z_{N+1}^2 \sigma_{\mathrm{angle,u}}^2, & i = N+1. \end{cases} \tag{9}$$

Based on the radial displacement model in (8), the PDF of $h_i^{(\mathrm{pe})}$ is written as [20]

$$f_{h_i^{(\mathrm{pe})}}\left(h_i^{(\mathrm{pe})}\right) = \frac{\zeta_i^2}{A_i^{\zeta_i^2}} (h_i^{(\mathrm{pe})})^{\zeta_i^2 - 1}, \quad 0 \leq h_i^{(\mathrm{pe})} \leq A_i, \quad i = 1, \cdots, N+1, \tag{10}$$

where $A_i = [\mathrm{erf}(v_i)]^2$ is the fraction of the collected power when $r_{\mathrm{tr},i} = 0$, $v_i = \sqrt{\pi} r_a / \left(\sqrt{2} w_{z,i}\right)$ is the ratio between the aperture radius and the beam width. $\zeta_i^2 = w_{z_{\mathrm{eq}},i}^2 / 4\sigma_{\mathrm{s},i}^2$ is the ratio between the squared equivalent beam width and displacement variance, where $\omega_{z_{\mathrm{eq}},i}^2 = \omega_{z,i}^2 \sqrt{\pi} \mathrm{erf}(v_i) / (2\ v_i e^{-v^2}) \approx \omega_{z,i}^2 + 3/(2\sqrt{2})$ is the equivalent beam width [30].

4) Link Interruption Due to AoA Fluctuation: As depicted in Fig. 3, due to the effect of AoA fluctuation, the beam is no longer orthogonal to the receiver plane. When an incident laser with $\theta_{\mathrm{a},i}$ arrives at the receiving plane, the airy pattern may be out of detector range occasionally due to the relatively large orientation deviations of hovering UAV, and the case that received AoA exceeds the range of FoV will result in an outage. Here, the AoAs for different links are defined as [18]

$$\theta_{\mathrm{a},i} \simeq \begin{cases} \sqrt{\theta_{\mathrm{rx},i}^2 + \theta_{\mathrm{ry},i}^2}, & i = 1 \\ \sqrt{\left(\theta_{\mathrm{tx},i} + \theta_{\mathrm{rx},i}\right)^2 + \left(\theta_{\mathrm{ty},i} + \theta_{\mathrm{ry},i}\right)^2}, & i = 2, \ldots, N \\ \sqrt{\theta_{\mathrm{tx},i}^2 + \theta_{\mathrm{ty},i}^2}, & i = N+1, \end{cases} \tag{11}$$

where $\theta_{\mathrm{tx},i}$ and $\theta_{\mathrm{ty},i}$ are the horizontal and vertical misalignment orientations of the transmitter in the ith link. Similarly, $\theta_{\mathrm{rx},i}$ and $\theta_{\mathrm{ry},i}$ represent the horizontal and vertical orientation deviations of the receiver. Therefore, $\theta_{\mathrm{a},i}$, $i = 1, \cdots, N+1$

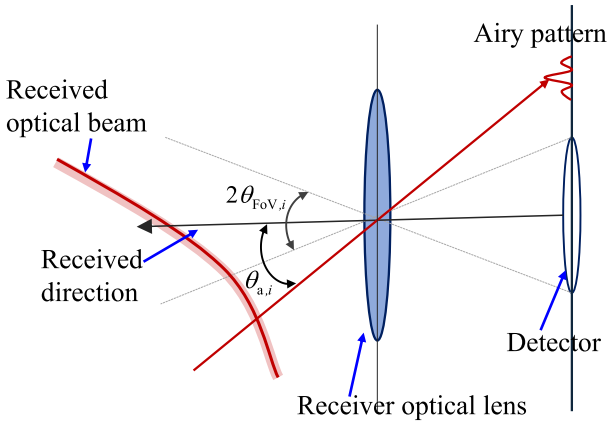

Fig. 3. A schematic diagram about the impact of AoA fluctuation for the ith link.

is Rayleigh-distributed, i.e.,

$$f_{\theta_{\mathrm{a},i}}(\theta_{\mathrm{a},i}) = \frac{\theta_{\mathrm{a},i}}{m_i \sigma^2_{\mathrm{angle,u}}} \exp\left(-\frac{\theta^2_{\mathrm{a},i}}{2m_i\sigma^2_{\mathrm{angle,u}}}\right), \quad \theta_{\mathrm{a},i} \geq 0, \tag{12}$$

where m_i varies with the type of links and is given by

$$m_i = \begin{cases} 1, & i = 1 \text{ or } N+1 \\ 2, & i = 2, \ldots, N. \end{cases} \tag{13}$$

We focus on the main lobe of the airy pattern, which has the most power. The width of the main lobe is approximately equal to 2.4λ, which is much smaller than the typical detector size [31]. Consequently, a reasonable consideration is the zero-one distribution that describes whether the incident laser is located on the receiving FoV or not [32]. Mathematically, given a fixed FoV, the link interruption (i.e., $h_i^{(\mathrm{aoa})} = 0$) occurs if $\theta_{\mathrm{a},i} > \theta_{\mathrm{FoV},i}$, and the maximum signal power (i.e., $h_i^{(\mathrm{aoa})} = 1$) is collected otherwise. Therefore, the corresponding PDF of $h_i^{(\mathrm{aoa})}$ is given by

$$f_{h_i^{(\mathrm{aoa})}}(h_i^{(\mathrm{aoa})}) = \exp\left(-\frac{\theta^2_{\mathrm{FoV},i}}{2m_i\sigma^2_{\mathrm{angle,u}}}\right)\delta(h_i^{(\mathrm{aoa})}) + \left[1-\exp\left(-\frac{\theta^2_{\mathrm{FoV},i}}{2m_i\sigma^2_{\mathrm{angle,u}}}\right)\right]\delta(h_i^{(\mathrm{aoa})}-1), \quad i = 1, \cdots, N+1. \tag{14}$$

III. Outage Performance Analysis

In this section, the overall statistical characteristic of the FSO channel is analyzed. Then, the link outage probability and the end-to-end outage probability are derived. Finally, the asymptotic behaviors of the outage probabilities are studied. Some insights are provided as well.

A. Overall Channel Statistical Characteristic

For the four impairments in (3), $h_i^{(\mathrm{l})}$ and $h_i^{(\mathrm{a})}$ are obviously independent and also independent of $h_i^{(\mathrm{pe})}$ and $h_i^{(\mathrm{aoa})}$. Although the orientation deviations of the transmitters (i.e., $\theta_{\mathrm{tx},i}$ and $\theta_{\mathrm{ty},i}$) contribute to the pointing error and the AoA fluctuation simultaneously, the correlation between $h_i^{(\mathrm{pe})}$ and $h_i^{(\mathrm{aoa})}$ is weak when $\theta_{\mathrm{FoV},i} \gg \sigma_{\mathrm{angle,u}}$. The reason is provided as follows. Note that $\sigma_{\mathrm{angle,u}}$ is the standard deviation of $\theta_{\mathrm{tx},i}$ and $\theta_{\mathrm{ty},i}$. Under a small value of $\sigma_{\mathrm{angle,u}}$ relative to $\theta_{\mathrm{FoV},i}$, compared with $\mathbf{r}_{\mathrm{t},i}$ and $\mathbf{r}_{\mathrm{r},i}$, the impact of $\mathbf{r}_{\theta_{\mathrm{t},i}} \simeq [Z_i\theta_{\mathrm{tx},i}, Z_i\theta_{\mathrm{ty},i}]$ in Fig. 2 on pointing error is weak. This indicates that the transmitter's orientation misalignment is weakly correlated with pointing error when $\theta_{\mathrm{FoV},i} \gg \sigma_{\mathrm{angle,u}}$. Moreover, when $\theta_{\mathrm{FoV},i} \gg \sigma_{\mathrm{angle,u}}$, $\theta_{\mathrm{tx},i}$ and $\theta_{\mathrm{ty},i}$ have little effect on $\theta_{\mathrm{a},i}$, and thus the transmitter's orientation misalignment and the AoA fluctuation are also weakly correlated. Consequently, the four impairments in (3) can be approximated as independent variables. Specially, for the GU link, the pointing error and the AoA fluctuation are no longer relevant since orientation deviations of the source node are approximately zero, and these four impairments are practically independent.

According to the above analysis, the PDF of h_i is approximated as

$$f_{h_i}(h_i) \simeq \int_0^{+\infty} \frac{1}{h_i'} f_{h_i^{(\mathrm{aoa})}}\left(\frac{h_i}{h_i'}\right) f_{h_i'}(h_i')\,\mathrm{d}h_i', \tag{15}$$

where $h_i' \triangleq h_i^{(\mathrm{l})} h_i^{(\mathrm{a})} h_i^{(\mathrm{pe})}$. By solving (15), we derive the PDF of h_i and state the result in the following theorem.

Theorem 1: For the UAV-based FSO communication system, the PDF of the overall channel gain h_i is approximated as

$$f_{h_i}(h_i) \simeq \exp\left(-\frac{\theta^2_{\mathrm{FoV},i}}{2m_i\sigma^2_{\mathrm{angle,u}}}\right)\delta(h_i) + \left[1-\exp\left(-\frac{\theta^2_{\mathrm{FoV},i}}{2m_i\sigma^2_{\mathrm{angle,u}}}\right)\right]\frac{\alpha_i\beta_i\zeta_i^2}{A_i h_i^{(\mathrm{l})}\Gamma(\alpha_i)\Gamma(\beta_i)} \times G_{1,3}^{3,0}\left[\frac{\alpha_i\beta_i}{A_i h_i^{(\mathrm{l})}} h_i \middle| \begin{matrix} \zeta_i^2 \\ \zeta_i^2 - 1, \alpha_i - 1, \beta_i - 1 \end{matrix}\right]. \tag{16}$$

Proof: See Appendix A. ∎

To verify the accuracy of the approximated PDF expression in *Theorem 1*, we provide Fig. 4 in Section V. As can be seen, the approximate PDF in (16) is tight as long as $\theta_{\mathrm{FoV},i} \geq 5\sigma_{\mathrm{angle,u}}$, which justifies the proposed approximation.

B. Link Outage Probability

1) Exact Expression: The outage probability is an important metric to evaluate the performance of the FSO communication system. The outage probability of the ith link p_i is expressed as the probability that the instantaneous SNR Υ_i falls below the specified threshold Υ_{th}, i.e.,

$$p_i = \Pr(\Upsilon_i < \Upsilon_{\mathrm{th}}) = \Pr(h_i < h_{\mathrm{th},i}), \tag{17}$$

where the corresponding threshold of the channel gain is

$$h_{\mathrm{th},i} = \sqrt{\frac{\Upsilon_{\mathrm{th}}\sigma^2_{\mathrm{n},i}}{2R^2P_{\mathrm{t}}^2}} = \frac{\theta_{\mathrm{FoV},i}}{RP_{\mathrm{t}}}\sqrt{\frac{\Upsilon_{\mathrm{th}}\Lambda}{2}}. \tag{18}$$

The exact expression of (17) is provided in the following theorem.

Theorem 2: For the UAV-based FSO communication system, the exact expression of the link outage probability p_i, $i = 1, \ldots, N+1$ is given by

$$p_i = \exp\left(-\frac{\theta_{\mathrm{FoV},i}^2}{2m_i\sigma_{\mathrm{angle,u}}^2}\right) + \left[1 - \exp\left(-\frac{\theta_{\mathrm{FoV},i}^2}{2m_i\sigma_{\mathrm{angle,u}}^2}\right)\right] \times \frac{\zeta_i^2}{\Gamma(\alpha_i)\Gamma(\beta_i)} G_{2,4}^{3,1}\left[\frac{\alpha_i\beta_i\theta_{\mathrm{FoV},i}}{A_i h_i^{(\mathrm{l})} R P_{\mathrm{t}}}\sqrt{\frac{\Upsilon_{\mathrm{th}}\Lambda}{2}}\,\middle|\, \begin{matrix} 1, \zeta_i^2+1 \\ \zeta_i^2, \alpha_i, \beta_i, 0 \end{matrix}\right], \tag{19}$$

where m_i is given by (13).

Proof: See Appendix B. ∎

2) Asymptotic Bound: For large transmit power P_{t}, the asymptotic bound of the link outage probability is given in the following theorem.

Theorem 3: For the UAV-based FSO communication system, the asymptotic bound of the link outage probability $p_{\mathrm{bound},i}$, $i = 1, \ldots, N+1$ for large transmit power P_{t} is given by

$$p_{\mathrm{bound},i} = \exp\left(-\frac{\theta_{\mathrm{FoV},i}^2}{2m_i\sigma_{\mathrm{angle,u}}^2}\right). \tag{20}$$

Proof: See Appendix C. ∎

Remark 1: In *Theorem 3*, the asymptotic bound (20) varies with $\theta_{\mathrm{FoV},i}^2$ and m_i. From (13), it is known that $m_i = 1$ for the UG/GU link, while $m_i = 2$ for the UU links. Given a fixed $\theta_{\mathrm{FoV},i}^2$ for all the links, the asymptotic bound (20) for the UU links is larger than that for the GU/UG link, the asymptotic bound (20) for the GU link is the same as that for the UG link, which indicates that the UU links achieve the worst asymptotic outage performance, and the GU link and the UG link achieve the same asymptotic outage performance.

C. End-to-End Outage Probability

1) Exact Expression: For DF relaying, outage of each intermediate link may lead to the outage of the relaying system. Therefore, the end-to-end outage probability is given by

$$P^{\mathrm{out}} = 1 - \prod_{i=1}^{N+1}(1 - p_i). \tag{21}$$

Then, the end-to-end outage probability is obtained in the following theorem.

Theorem 4: For the UAV-based FSO communication system, the exact expression of the end-to-end outage probability P^{out} is expressed as

$$\begin{aligned} P^{\mathrm{out}} &= 1 - \left[1 - \exp\left(-\frac{\theta_{\mathrm{FoV},1}^2}{2\sigma_{\mathrm{angle,u}}^2}\right)\right] \times \left[1 - \exp\left(-\frac{\theta_{\mathrm{FoV},N+1}^2}{2\sigma_{\mathrm{angle,u}}^2}\right)\right] \prod_{i=2}^{N}\left[1 - \exp\left(-\frac{\theta_{\mathrm{FoV},i}^2}{4\sigma_{\mathrm{angle,u}}^2}\right)\right] \\ &\quad \times \prod_{i=1}^{N+1}\left(1 - \frac{\zeta_i^2}{\Gamma(\alpha_i)\Gamma(\beta_i)} G_{2,4}^{3,1}\left[\frac{\alpha_i\beta_i}{A_i h_i^{(\mathrm{l})}} h_{\mathrm{th},i}\,\middle|\, \begin{matrix} 1, \zeta_i^2+1 \\ \zeta_i^2, \alpha_i, \beta_i, 0 \end{matrix}\right]\right). \end{aligned} \tag{22}$$

Proof: The proof is straightforward by submitting (19) into (21). ∎

2) Asymptotic Bound: Due to the impact of the intermediate links performance bound in (20), the corresponding system performance is also limited by AoA fluctuation when the transmitted power is large. The asymptotic bound for the end-to-end outage probability is given in the following theorem.

Theorem 5: For the UAV-based FSO communication system, the asymptotic bound of the end-to-end outage probability $P_{\mathrm{bound}}^{\mathrm{out}}$ for large transmit power P_{t} is given by

$$\begin{aligned} P_{\mathrm{bound}}^{\mathrm{out}} &= 1 - \left[1 - \exp\left(-\frac{\theta_{\mathrm{FoV},1}^2}{2\sigma_{\mathrm{angle,u}}^2}\right)\right] \times \left[1 - \exp\left(-\frac{\theta_{\mathrm{FoV},N+1}^2}{2\sigma_{\mathrm{angle,u}}^2}\right)\right] \\ &\quad \times \prod_{i=2}^{N}\left[1 - \exp\left(-\frac{\theta_{\mathrm{FoV},i}^2}{4\sigma_{\mathrm{angle,u}}^2}\right)\right]. \end{aligned} \tag{23}$$

Proof: The proof is straightforward by substituting (20) into (21). ∎

Remark 2: It is worth mentioning that the asymptotic bound $P_{\mathrm{bound}}^{\mathrm{out}}$ in (23) deteriorates with the increase of the number of relays N. Interestingly, increasing relay number worsens the outage performance when the system outage performance has attained the bound in (23).

IV. Parameter Optimizations

In this section, the key parameter optimizations for the UAV-based FSO communications are investigated. Specifically, the beam width, the FoV, and the UAV locations are optimized.

A. Beam Width Adjustment

Since hovering UAVs have larger deviations of the position and orientation than fixed ground platforms, pointing error in UAV-based links is more severe, hence the adjustment for beam width is especially important to improve the diversity order gain and outage performance for different communication conditions.

In (10), the ratio between the squared equivalent beam width and displacement variance is $\zeta_i^2 = {w_z}_{\mathrm{eq},i}^2/(4\sigma_{\mathrm{s},i}^2) \approx [\omega_{z,i}^2 + 3/(2\sqrt{2})]/(4\sigma_{\mathrm{s},i}^2)$. In (5), β_i denotes the parameters related to small-scale eddy in atmospheric turbulence. According to [30] and [33], it can be known that the condition $\zeta_i^2 < \beta_i$ represents that pointing error becomes dominant in relation to atmospheric turbulence in the ith link. Since the turbulence parameter β_i, which is related to the atmospheric condition, cannot be chosen arbitrarily, adjusting beam width $w_{z,i}$ to satisfy $\zeta_i^2 \geq \beta_i$ is an appropriate measure. By letting $\zeta_i^2 = \beta_i$, the minimum value of received beam width in the ith link is given by

$$\omega_{z,i}^{\min} = \sqrt{4\beta_i\sigma_{\mathrm{s},i}^2 - \frac{3}{2\sqrt{2}}}. \tag{24}$$

Here, to avoid the severe impairment of pointing error, the beam width of each link in the FSO relaying system should satisfy

$$\omega_{z,i} \geq \omega_{z,i}^{\min}, \quad i = 1, \cdots, N+1. \tag{25}$$

It is noteworthy to mention that the power received at fixed-size detector reduces with an increase of the beam width. Consequently, excessive increase of the beam width is also inadvisable.

B. FoV Optimization With the Beam Width Constraint

Due to the asymptotic bound (23), the achievable end-to-end outage probability is limited. Therefore, after determining the minimum beam width, the FoV optimization problem should be considered to minimize the end-to-end outage probability, i.e.,

$$\begin{aligned} \min_{\theta_{\mathrm{FoV},1},\ldots,\theta_{\mathrm{FoV},N+1}} \quad & P^{\mathrm{out}} \\ \text{s.t. } & \omega_{z,i} \geq \omega_{z,i}^{\min}, \quad i = 1, \ldots, N+1. \end{aligned} \tag{26}$$

Since FoV adjustment of one link does not affect the other links, problem (26) is reduced to optimizing FoV of each link individually, i.e.,

$$\begin{aligned} \min_{\theta_{\mathrm{FoV},i}} \quad & p_i \\ \text{s.t. } & \omega_{z,i} \geq \omega_{z,i}^{\min}. \end{aligned} \tag{27}$$

Considering the complexity of the exact link outage probability and the demand of practical FSO communications, we optimize the system performance for large P_{t}. By substituting (2) and (18) into (C.2), we obtain the link outage probability for large P_{t} with respect to $\theta_{\mathrm{FoV},i}$ as

$$p_i \simeq L(\theta_{\mathrm{FoV},i}^2) + \Theta\left[1 - L(\theta_{\mathrm{FoV},i}^2)\right](\theta_{\mathrm{FoV},i})^{\beta_i}, \tag{28}$$

where $L(\theta_{\mathrm{FoV},i}^2)$ and Θ are defined as

$$\begin{cases} L(\theta_{\mathrm{FoV},i}^2) = \exp\left(-\dfrac{\theta_{\mathrm{FoV},i}^2}{2m_i\sigma_{\mathrm{angle,u}}^2}\right) \\ \Theta = \dfrac{\zeta_i^2\Gamma(\alpha_i-\beta_i)}{\Gamma(\alpha_i)\Gamma(\beta_i)(\zeta_i^2-\beta_i)\beta_i}\left(\dfrac{\alpha_i\beta_i}{A_i h_i^{(1)} R P_{\mathrm{t}}}\sqrt{\dfrac{\Upsilon_{\mathrm{th}}\Lambda}{2}}\right)^{\beta_i}. \end{cases} \tag{29}$$

By taking derivative of (28) with respect to $\theta_{\mathrm{FoV},i}$ and setting it to be zero, we obtain the following nonlinear equation

$$\begin{aligned} m_i\Theta\sigma_{\mathrm{angle,u}}^2\beta_i(\theta_{\mathrm{FoV},i})^{\beta_i-2}\left[1 - L\left(\theta_{\mathrm{FoV},i}^2\right)\right] \\ + \Theta(\theta_{\mathrm{FoV},i})^{\beta_i} L'\left(\theta_{\mathrm{FoV}_i}^2\right) - L'\left(\theta_{\mathrm{FoV},i}^2\right) = 0. \end{aligned} \tag{30}$$

In this paper, the asymptotically optimal $\theta_{\mathrm{FoV},i}$ is updated to match different communication conditions by numerically solving (30).

C. UAV Location Optimization

To improve the reliability of the end-to-end link, the UAVs' positions can be optimized. To avoid the undesirable bound of AoA fluctuation (i.e. eq. (20)), the FoV of each receiver is typically set to be a large fixed value. In this subsection, we assume that the FoV is sufficiently large so that the AoA fluctuation is neglectable.

Here, we consider an FSO relaying system with N UAVs and N_0 obstacles. To facilitate the optimization, all UAVs are assumed to be located at the same height. For all UAVs, the two-dimensional coordinates in the XY plane are optimized. Without loss of generality, the positions of UAVs are set to be $(x_i, y_i), i = 1, \cdots, N$. Moreover, (x_0, y_0) and (x_{N+1}, y_{N+1}) are the coordinates of source node and destination node, respectively. Due to the existence of obstacles, the UAVs cannot be deployed on the positions of obstacles. An indicator function $f_n(x_i, y_i, x_{i+1}, y_{i+1})$ is used to indicate whether the ith link is block by the nth obstacle. Specifically, if the nth obstacle blocks the ith link, $f_n(x_i, y_i, x_{i+1}, y_{i+1}) \geq 0$, otherwise $f_n(x_i, y_i, x_{i+1}, y_{i+1}) < 0$. Here, the UAV location optimization problem can be formulated as

$$\begin{aligned} \min_{x_1,y_1,\ldots,x_N,y_N} \quad & P^{\mathrm{out}} \\ \text{s.t. } & f_n(x_i, y_i, x_{i+1}, y_{i+1}) < 0, \\ & i \in 0, 1, \cdots, N; \quad n \in 1, 2, \cdots, N_0. \end{aligned} \tag{31}$$

To solve the optimization problem, we assume that the atmospheric turbulence is dominant in relation to the pointing error (i.e., $\zeta_i^2 > \beta_i, i = 1, \cdots, N+1$), and the FoV $\theta_{\mathrm{FoV},i}$ is large. With these assumptions, the expression (C.2) can be further written as

$$\begin{aligned} p_i &\approx \frac{\zeta_i^2\Gamma(\alpha_i-\beta_i)}{\Gamma(\alpha_i)\Gamma(\beta_i)(\zeta_i^2-\beta_i)\beta_i}\left(\frac{\alpha_i\beta_i}{A_i h_i^{(1)}}\right)^{\beta_i}\left(h_{\mathrm{th},i}\right)^{\beta_i} \\ &= \underbrace{\frac{\zeta_i^2\Gamma(\alpha_i-\beta_i)}{\Gamma(\alpha_i)\Gamma(\beta_i)(\zeta_i^2-\beta_i)\beta_i}\left(\frac{\alpha_i\beta_i}{A_i h_i^{(1)} R}\sqrt{\frac{\Upsilon_{\mathrm{th}}\sigma_{\mathrm{n},i}^2}{2}}\right)^{\beta_i}}_{\triangleq a_i} \\ &\quad \times (P_{\mathrm{t}})^{-\beta_i}. \end{aligned} \tag{32}$$

We assume that the $i_{\max}$th link is the longest with parameters $a_{i_{\max}}$ and $\beta_{i_{\max}}$. Since the parameter β_i decreases monotonically with an increase of the ith link distance, we have

$$\begin{aligned} \lim_{P_{\mathrm{t}}\to\infty}\frac{1-\prod_{i=1}^{N+1}(1-p_i)}{p_{i_{\max}}} &= \lim_{P_{\mathrm{t}}\to\infty}\frac{\sum_{i=1}^{N+1}p_i}{p_{i_{\max}}} \\ &= \lim_{P_{\mathrm{t}}\to\infty}\frac{\sum_{i=1}^{N+1}a_i P_{\mathrm{t}}^{-\beta_i}}{a_{i_{\max}}P_{\mathrm{t}}^{-\beta_{i_{\max}}}} \\ &= 1, \end{aligned} \tag{33}$$

which indicates that the system outage probability is determined by the performance of the link having the maximum distance. Therefore, for a large value of P_{t}, problem (31) can

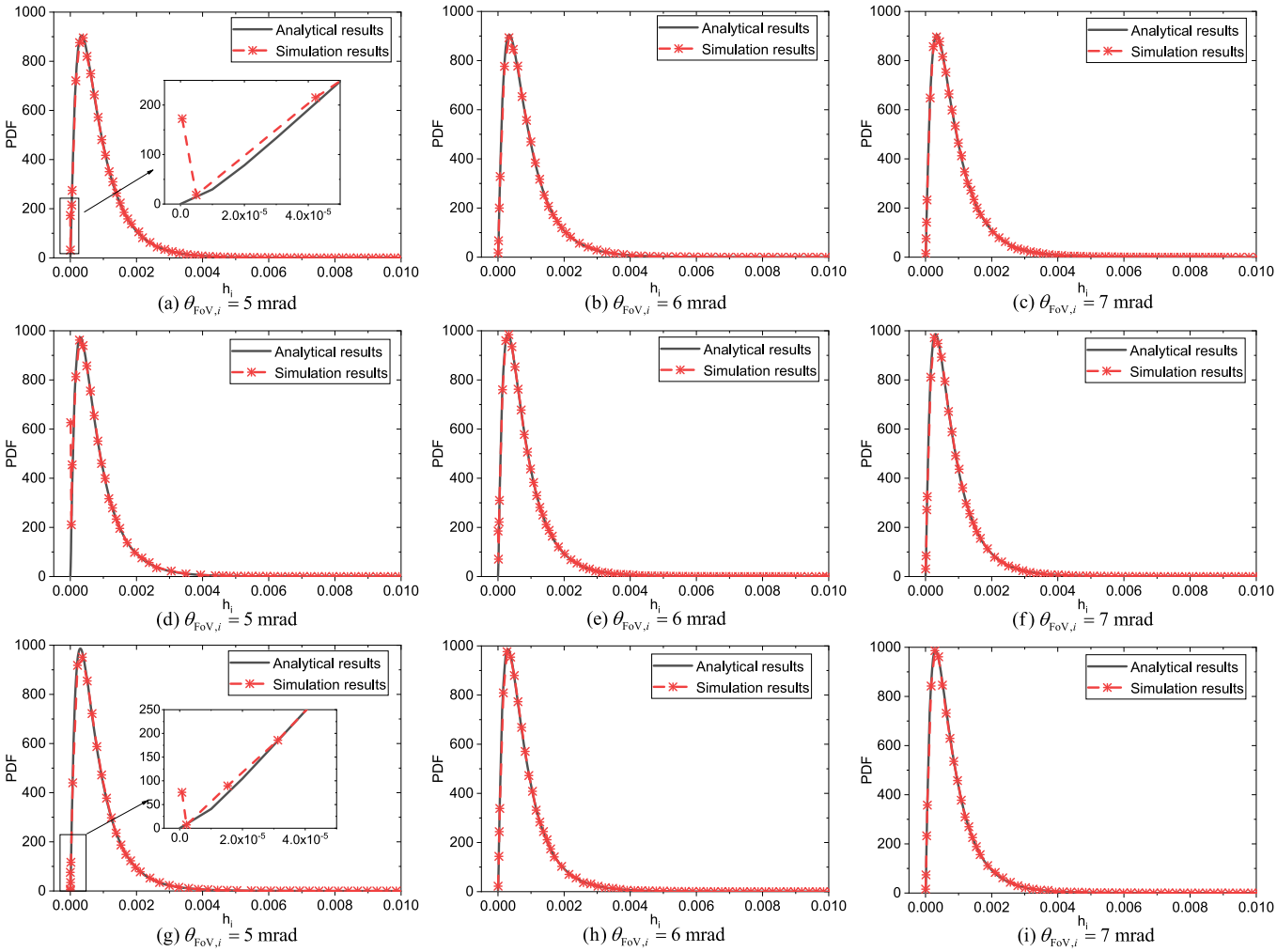

Fig. 4. Comparisons of the derived PDF (16) and the simulated PDF with different $\theta_{\mathrm{FoV},i}$ for different links when $Z_i = 250$ m and $w_{z_i} = 2$ m, where (a)-(c) are for the GU link, (d)-(f) are for the UU links, (g)-(i) are for the UG link.

be transformed into

$$\begin{aligned} \min_{x_1,y_1,\cdots,x_N,y_N} \quad & \max\{Z_1, Z_2, \cdots, Z_N\} \\ \text{s.t.} \quad & f_n(x_i, y_i, x_{i+1}, y_{i+1}) < 0 \\ & i \in 0, 1, \cdots, N; \quad n \in 1, 2, \cdots, N_0, \end{aligned} \tag{34}$$

where $Z_i = \sqrt{(x_i - x_{i+1})^2 + (y_i - y_{i+1})^2}$ is the distance of the ith link. To solve problem (34) effectively, the grouping optimization or multi-variate optimization can be used, which can be implemented by using the embedded function "fmincon" in MATLAB [25].

V. Numerical Results

In this section, some numerical results will be presented to support the theoretical claims made in previous sections. Unless stated otherwise, the default values of the parameters used for simulations are given by $\lambda = 1550$ nm, $C_n^2 = 5 \times 10^{-14}$ m$^{-2/3}$, $R = 0.9$, $\Phi = 1$ km^{-1}, $\sigma_{\mathrm{n}}^2 = 6.4 \times 10^{-14}$ corresponding to $\theta_{\mathrm{FoV},i} = 8$ mrad, receiver lens radius $r_a = 5$ cm, the standard deviation of UAV and ground displacement $\sigma_{\mathrm{p,u}} = \sigma_{\mathrm{p,g}} = 10$ cm, the standard deviation of UAV orientation $\sigma_{\mathrm{angle,u}} = 1.2$ mrad, and $\gamma_{\mathrm{th}} = 10$ dB [18].

A. Channel Modelling Results

The derivation of the PDF in (16) is based on the assumption that the four types of impairments in (3) are independent of each other. To verify the accuracy of (16), we compare the curves of (16) with the simulated PDFs for different links when $Z_i = 250$ m and $w_{z_i} = 2$ m, as shown in Fig. 4. Note that Figs. 4(a)-(c) are for the GU link, Figs. 4(d)-(f) are for the UU links, and Figs. 4(g)-(i) are for the UG link. For the simulated PDFs, the four impairments in (3) are set to be correlated random variables. As can be seen in Figs. 4(a), (d) and (g), when $\theta_{\mathrm{FoV},i} = 5$ mrad, the differences between analytical results when $h_i = 0$ and simulation results are large. Specifically, for the GU, UU and UG links, $f_{h_i}(0)$ in (16) are 1.3×10^{-2}, 1.7×10^{-4} and 1.7×10^{-4}, respectively. But the simulated values at $h_i = 0$ are 172.7, 626.6, and 75.6, respectively. For other values of h_i in Fig. 4(a), (d) and (g), the analytical results match the simulation results well. This indicates that small FoV in each link will result in the

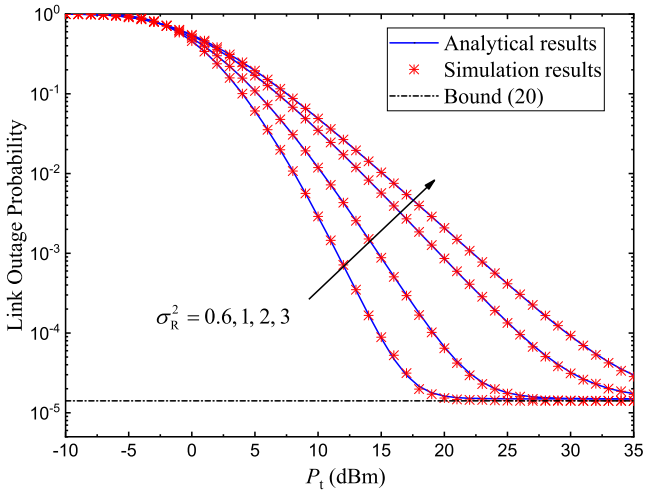

Fig. 5. Link outage probability for an UU link versus average transmitted optical power under different turbulence conditions when $\theta_{\mathrm{FoV}} = 8$ mrad, $w_z = 2$ m and $Z = 250$ m.

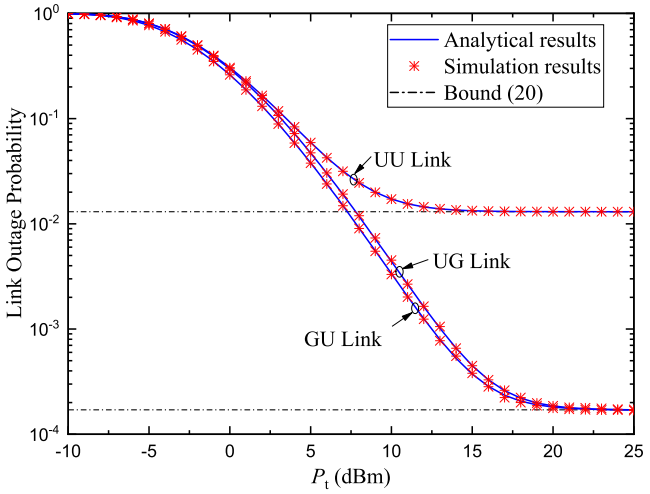

Fig. 6. Link outage probability versus average transmitted optical power for different kinds of links when $\theta_{\mathrm{FoV},i} = 5$ mrad, $\sigma_{\mathrm{R},i}^2 = 1$, $w_{z,i} = 2$ m and $Z_i = 250$ m.

mismatch between the analytical results and simulation results when $h_i = 0$. When $\theta_{\mathrm{FoV},i} \geq 6$ mrad (i.e., $\theta_{\mathrm{FoV},i} \geq 5\sigma_{\mathrm{angle,u}}$), as shown in Figs. 4(b), (c), (e), (f), (h) and (i), the analytical curves match the simulation results well. This indicates that the derived tractable expression (16) is accurate when $\theta_{\mathrm{FoV},i}$ is large and can be directly used for performance analysis.

B. Performance Analysis Results

In this subsection, we will examine the accuracy of the derived link outage probability and the end-to-end outage probability under different scenarios.

Fig. 5 plots the link outage probability for a UU link versus the average transmitted optical power P_{t} under different turbulence conditions $\sigma_{\mathrm{R}}^2 = 0.6, 1, 2, 3$ when $\theta_{\mathrm{FoV}} = 8$ mrad, $w_z = 2$ m and $Z = 250$ m. For comparison, the asymptotic bound (20) in *Theorem 3* is also presented. For small P_{t}, the values of link outage probabilities decrease with the increase of P_{t} or with the decrease of σ_{R}^2. For large P_{t}, the values of link outage probabilities tend to stable values, which are independent of the average transmitted optical power and the turbulence condition. Moreover, the stable values approach the asymptotic bound (20). This verifies the accuracy of (20) in *Theorem 3*. Moreover, it should be emphasized that all analytical results in Fig. 5 present close agreement with Monte-Carlo simulation results, and the accuracy of the derived expression (19) in *Theorem 2* is verified.

Fig. 6 compares the link outage performance for different kinds of links when $\theta_{\mathrm{FoV},i} = 5$ mrad, $\sigma_{\mathrm{R},i}^2 = 1$, $w_{z,i} = 2$ m and $Z_i = 250$ m. In addition to obtaining the similar conclusions in Fig. 5, some other interesting insights can also be found in Fig. 6. As shown in Fig. 6, the UU link achieves the maximum link outage probability, and the GU link achieves the comparable performance to the UG link. Moreover, the GU link achieves the same asymptotic outage performance as the UG link, and the asymptotic bound of the UU link is always larger than that of the UG/GU link. These insights verify the analysis in *Remark 1*.

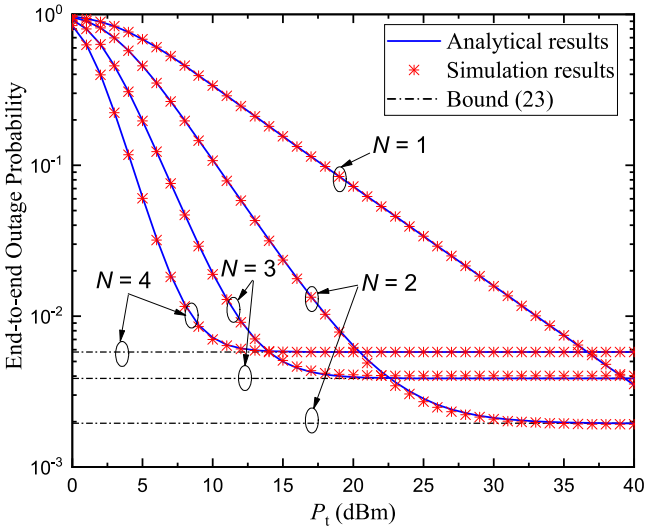

Fig. 7. End-to-end outage probability versus average transmitted optical power for different numbers of relays when $\theta_{\mathrm{FoV},i} = 6$ mrad, $w_{z,i} = 2$ m and the distance between source and destination nodes $Z_{\mathrm{SD}} = 2$ km.

Fig. 7 shows the end-to-end outage probability versus the average transmitted optical power P_{t} for different numbers of relays N when $\theta_{\mathrm{FoV},i} = 6$ mrad, $w_{z,i} = 2$ m and the distance between source and destination nodes $Z_{\mathrm{SD}} = 2$ km. For comparison, the asymptotic bound (23) in *Theorem 5* is also presented. In this simulation, the obstacles are not considered, and N UAV nodes are uniformly deployed between the source node and the destination node. For small P_{t}, the end-to-end outage probability performance improves with the increase of P_{t} or N. However, at large P_{t}, the outage performance does not improve with P_{t}, but approaches the asymptotic bound (23), which verifies the accuracy of (23) in *Theorem 5*. Moreover, the asymptotic bound (23) varies with N. Specifically, the asymptotic bound with $N = 4$ achieves the largest value,

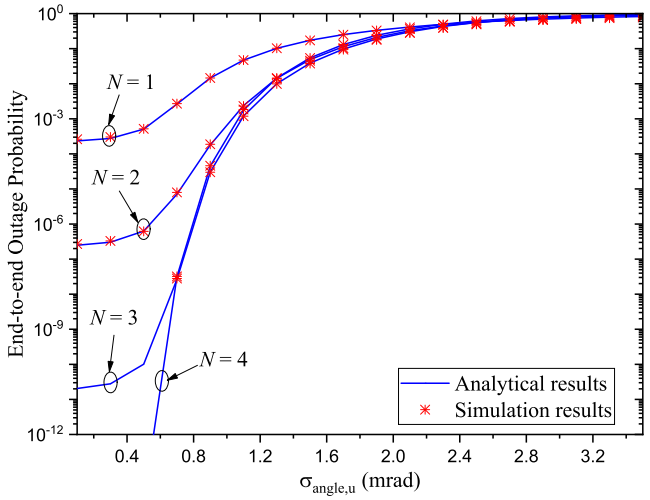

Fig. 8. End-to-end outage probability versus the standard deviation $\sigma_{\text{angle,u}}$ with different numbers of relays when $P_{\text{t}} = 20$ dBm, $\theta_{\text{FoV},i} = 6$ mrad, $w_{\text{z},i} = 2$ m, and $Z_{\text{SD}} = 2$ km.

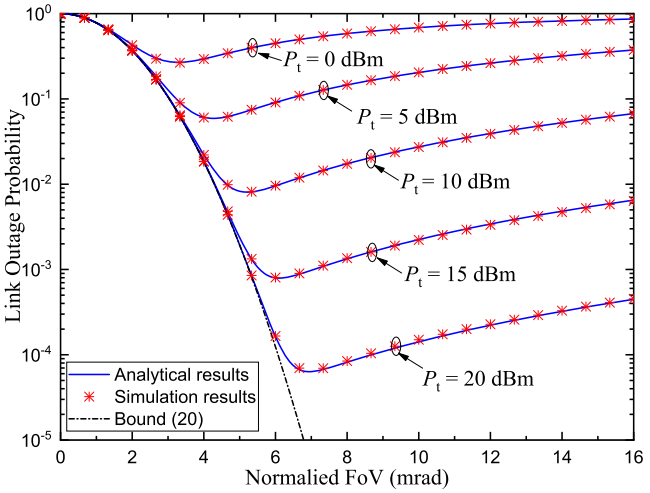

Fig. 9. Link outage probability of an UU link versus normalized FoV for different P_{t} when $Z = 250$ m and $w_z = 2$ m.

which coincides with the conclusion in *Remark 2*. Similar to Fig. 5, the accuracy of the derived expression of (22) in *Theorem 4* is also verified by using simulations.

Fig. 8 shows the end-to-end outage probability versus the standard deviation $\sigma_{\text{angle,u}}$ with different numbers of relays when $P_{\text{t}} = 20$ dBm, $\theta_{\text{FoV},i} = 6$ mrad, $w_{\text{z},i} = 2$ m, and $Z_{\text{SD}} = 2$ km. As can be observed, with the increase of $\sigma_{\text{angle,u}}$, the end-to-end outage probability increases sharply and then tends to one. This indicates that the system performance dramatically degrades with the increase of $\sigma_{\text{angle,u}}$. Moreover, a large $\sigma_{\text{angle,u}}$ (for example, $\geq$3.4 mrad) will directly result in a complete interruption of the system. Furthermore, when $\sigma_{\text{angle,u}}$ is small, the outage probability performance improves with the number of UAV relays. Therefore, the UAVs' orientation fluctuation and the number of relays are two major concerns for practical system design. In Fig. 8, all analytical results match well with simulation results, which also verifies the accuracy of the derived expression in (22).

C. Parameter Optimization Results

In this subsection, to verify the efficiency of the proposed optimization schemes, the parameter optimization results will be shown.

Fig. 9 shows the link outage probability of a UU link versus the normalized FoV ϕ_{FoV} for different P_{t} values when $Z = 250$ m and $w_z = 2$ m. Here, the normalized FoV is defined as $\phi_{\text{FoV}} = \theta_{\text{FoV}}/\sigma_{\text{angle,u}}$, and the beam width w_z is adjusted to satisfy (25). As can be seen, with the increase of P_{t}, the link outage probability performance improves. Moreover, all analytical results accurately match simulation results in the entire normalized FoV range, which verifies the accuracy of (19) in *Theorem 2*. All curves tend to the asymptotic bound in (20) with the decrease of ϕ_{FoV}, which indicates the correctness of *Theorem 3*. Furthermore, with the increase of ϕ_{FoV}, the link outage probability decreases first and then increases. It can be observed from Fig. 9 that, when

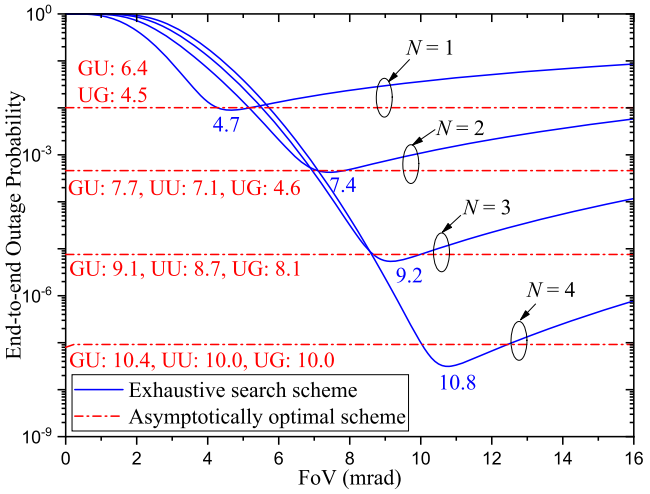

Fig. 10. End-to-end outage probability versus FoV with different numbers of relays when $P_{\text{t}} = 20$ dBm, $\sigma_{\text{angle,u}} = 1.2$ mrad, $\theta_{\text{FoV},i} = 6$ mrad, $w_{\text{z},i} = 4$ m, and $Z_{\text{SD}} = 2$ km.

$P_{\text{t}} = 0, 5, 10, 15$ and 20 dBm, the optimal values of ϕ_{FoV} (in mrad) are 3.25, 4.25, 5.25, 6.08, and 6.92, respectively. By solving (30), we obtain the corresponding asymptotically optimal ϕ_{FoV} values as 1.94, 3.67, 4.98, 6.02, and 6.91. The differences between the optimal ϕ_{FoV} in Fig. 9 and the asymptotically optimal ϕ_{FoV} using (30) are small when P_{t} is large. This indicates that, when P_{t} is large, eq. (30) can be directly used to determine the optimal FoV without time-consuming simulations.

Fig. 10 shows the end-to-end outage probability versus FoV with different numbers of relays when $P_{\text{t}} = 20$ dBm, $\sigma_{\text{angle,u}} = 1.2$ mrad, $\theta_{\text{FoV},i} = 6$ mrad, $w_{\text{z},i} = 4$ m, and $Z_{\text{SD}} = 2$ km. In Fig. 10, the obstacles are not considered, and the UAV relays are placed equidistant. The exhaustive search scheme and the asymptotically optimal scheme are provided. In the exhaustive search scheme, the FoVs for the GU, UG and UU links are set to be identical. In asymptotically optimal scheme, the optimal FoVs for all links are respectively

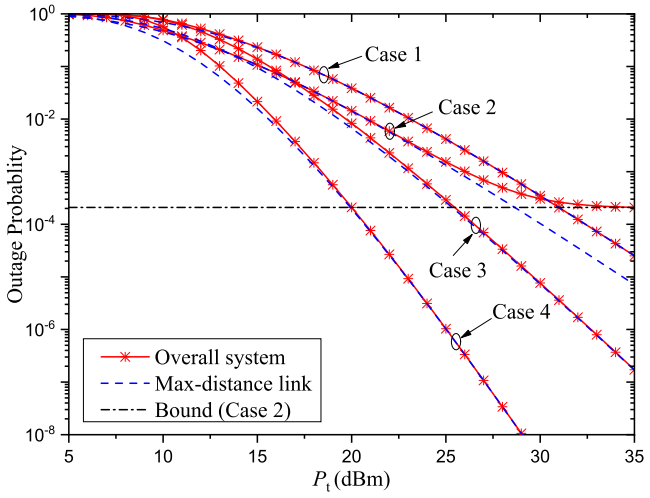

Fig. 11. Outage probability versus average link transmit power for different scenarios when $Z_{\rm SD} = 2$ km and $w_{z,i} = 4$ m.

obtained by (30). It can be seen that when FoV is increased, all curves of the exhaustive search scheme decrease first and then increase, this indicates that an optimal FoV exists for each curve. Specifically, for $N = 1, 2, 3$ and 4, the optimal FoVs in the exhaustive search scheme are 4.7 mrad, 7.4 mrad, 9.2 mrad, and 10.8 mrad, as marked on the figure. The corresponding minimum outage probabilities are 8.95×10^{-3}, 4.26×10^{-4}, 5.40×10^{-6}, and 3.13×10^{-8}, respectively. Moreover, the FoVs of different links for the asymptotically optimal scheme by using (30) are also provided on the figure. As seen, the asymptotically optimal scheme can achieve comparable outage performance to the exhaustive search scheme, which verifies the accuracy of (30).

To verify whether the link with maximum distance (i.e., max-distance link) dominates the end-to-end outage performance, Fig. 11 shows the outage probability versus average transmit power $P_{\rm t}$ for different scenarios when $Z_{\rm SD} = 2$ km and $w_{z,i} = 4$ m. In this simulation, the beam width satisfies $\zeta_i^2 > \beta_i, i = 1, \ldots, N+1$. Four cases are considered, as shown in Table I. Note that the asymptotic bounds for Cases 1 and 3 are 1.39×10^{-11}, the asymptotic bound for Case 4 is 2.78×10^{-11}, which are too small and not plotted in the figure. For cases with large FoV (i.e., Cases 1, 3 and 4) in Fig. 11, the outage probabilities of the max-distance link converge to that of the overall system when $P_{\rm t}$ is large (for example, when $P_{\rm t} \geq 12.5$ dBm for Case 1, when $P_{\rm t} \geq 27.5$ dBm for Case 3, or when $P_{\rm t} \geq 20$ dBm for Case 4), which verifies that the link with the maximum distance dominates the overall system performance, just as analyzed in (33). However, for the case with small FoV (i.e., Case 2), the outage probability of the max-distance link does not match with that of the overall system at large $P_{\rm t}$. In this case, the AoA fluctuation has a strong effect on outage performance. Moreover, the performance of Case 2 is better than that of Case 1 before reaching the asymptotic bound (23) since larger FoV introduces more background noise.

After optimizing the UAVs' locations, Fig. 12 and Fig. 13 show the deployment of UAVs under different scenarios.

TABLE I
THE SETUP OF FOUR CASES IN FIG. 11

Cases	Number of relays	Link distance (km)	FoV (mrad)
Case 1	2	$(Z_1, Z_2, Z_3) = (0.5, 0.5, 1)$	12
Case 2	2	$(Z_1, Z_2, Z_3) = (0.5, 0.5, 1)$	7
Case 3	2	$(Z_1, Z_2, Z_3) = (0.5, 0.7, 0.8)$	12
Case 4	3	$(Z_1, Z_2, Z_3, Z_4) = (0.4, 0.5, 0.5, 0.6)$	12

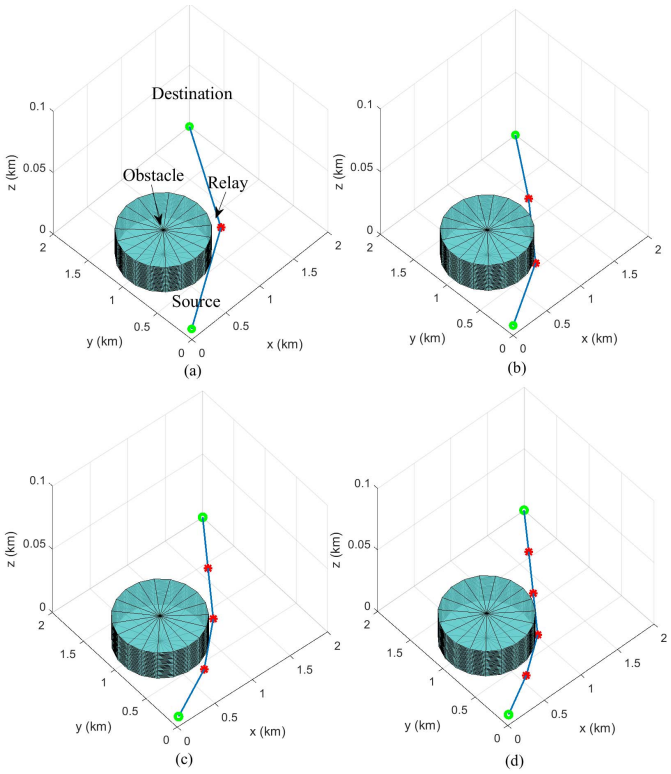

Fig. 12. Optimal relay deployment for the UAV-based FSO relaying system with one cylindrical obstacle. (a) one relay, (b) two relays, (c) three relays, (d) four relays.

TABLE II
THE OPTIMAL RELAY LOCATIONS AND LINK DISTANCES IN FIG. 12

Subfigures	Relay locations (in km)	Link distances (in km)
Fig. 12(a)	(1.2712, 0.8288)	1.3795, 1.3795
Fig. 12(b)	(0.8851, 0.5614), (1.4689, 1.2602)	0.9106, 0.9106, 0.9106
Fig. 12(c)	(0.7056, 0.4193), (1.2111, 0.8809), (1.6056, 1.4404)	0.6846, 0.6846, 0.6846, 0.6846
Fig. 12(d)	(0.5777, 0.3651), (1.0193, 0.6868), (1.3472, 1.1238), (1.6745, 1.5612)	0.5463, 0.5463, 0.5463, 0.5463, 0.5463

Specifically, Fig. 12 plots optimal relay deployment for the UAV-based FSO relaying system with one cylindrical obstacle. In the simulation, the coordinates of the source and the destination are (0.1 km, 0.1 km) and (2 km, 2 km). The obstacle is centered at (0.6 km, 1 km) with radius 0.5 km. From Fig. 12(a) to Fig. 12(d), the optimal locations of UAVs

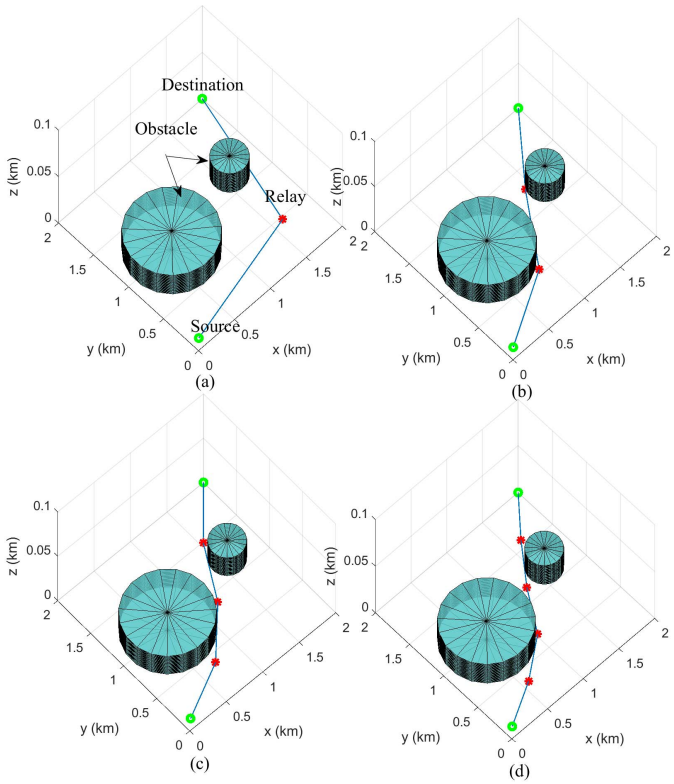

Fig. 13. Optimal relay deployment for the UAV-based FSO relaying system with two cylindrical obstacles. (a) one relay, (b) two relays, (c) three relays, (d) four relays.

TABLE III
THE OPTIMAL RELAY LOCATIONS AND LINK DISTANCES IN FIG. 13

Subfigures	Relay locations (in km)	Link distances (in km)
Fig. 13(a)	(1.2712, 0.8288)	1.3795, 1.3795
Fig. 13(b)	(0.8853, 0.5611), (1.4676, 1.2612)	0.9106, 0.9106, 0.9106
Fig. 13(c)	(0.7057, 0.4191), (1.2109, 0.8811), (1.6055, 1.4405)	0.6846, 0.6846, 0.6846, 0.6846
Fig. 13(d)	(0.5731, 0.3741), (1.0221, 0.6837), (1.3437, 1.1259), (1.6729, 1.5626)	0.5468, 0.5454, 0.5468, 0.5468, 0.5462

and link distances are listed in Table II. By adding another cylindrical obstacle at (1.6 km, 1.2 km) with radius 0.2 km, Fig. 13 shows the optimal relay deployment for the FSO relaying system. In this case, the optimal relay locations and link distances are provided in Table III. As can be seen from the above results, through optimizing the relays' deployment, the feasible positions of relays can always be found, and all link distances tend to be approximately equal.

VI. CONCLUSION

This paper investigated the channel modelling, outage probability analysis, and parameter optimization for UAV-based FSO relaying systems. A tractable and accurate channel model was established by taking into account atmospheric loss, atmospheric turbulence, pointing error, and link interruption due to AoA fluctuation. Based on the channel model, closed-form expressions were obtained for link outage probability and end-to-end outage probability. Subsequently, the asymptotic outage performance bounds were also investigated. Moreover, the beam width, FoV and UAVs' locations were optimized. Numerical results verify the accuracy of the derived theoretical expressions and the efficiency of the proposed optimization schemes. The obtained theoretical expressions enable designers to evaluate outage performance rapidly without time-intensive simulations. The derived parameter optimization results can help determine the optimal available parameter choices when designing the UAV-based FSO systems.

APPENDIX A
PROOF OF *Theorem 1*

By using (4), (5), (10) and expressing $K_n(\cdot)$ in terms of the Meijer's G-function [34], we can obtain the PDF of h_i' as [35]

$$f_{h_i'}\left(h_i'\right) = \frac{\alpha_i\beta_i\zeta_i^2}{A_i h_i^{(l)}\Gamma(\alpha_i)\Gamma(\beta_i)} \times G_{1,3}^{3,0}\left[\frac{\alpha_i\beta_i}{A_i h_i^{(l)}}h_i' \middle| \begin{matrix}\zeta_i^2 \\ \zeta_i^2-1, \alpha_i-1, \beta_i-1\end{matrix}\right]. \tag{A.1}$$

By substituting (14) and (A.1) into (15), we derive the PDF of h_i as

$$\begin{aligned} f_{h_i}\left(h_i\right) = {} & \exp\left(-\frac{\theta_{\mathrm{FoV},i}^2}{2m_i\sigma_{\mathrm{angle,u}}^2}\right)\int_0^\infty \frac{1}{h_i'}\delta\left(\frac{h_i}{h_i'}\right) f_{h_i'}\left(h_i'\right)\mathrm{d}h_i' \\ & + \left[1-\exp\left(-\frac{\theta_{\mathrm{FoV},i}^2}{2m_i\sigma_{\mathrm{angle,u}}^2}\right)\right] \\ & \times \int_0^\infty \frac{1}{h_i'}\delta\left(\frac{h_i}{h_i'}-1\right) f_{h_i'}\left(h_i'\right)\mathrm{d}h_i'. \end{aligned} \tag{A.2}$$

With $\delta(ax) = \delta(x)/|a|$ and $\int_{-\infty}^{\infty} f(a)\delta(x-a)\mathrm{d}a = f(x)$ [36], eq. (16) can be derived.

APPENDIX B
PROOF OF *Theorem 2*

By (16) and (17), p_i is given by

$$\begin{aligned} p_i = {} & \exp\left(-\frac{\theta_{\mathrm{FoV},i}^2}{2m_i\sigma_{\mathrm{angle,u}}^2}\right)\underbrace{\int_0^{h_{\mathrm{th},i}}\delta(h_i)\mathrm{d}h_i}_{=1} \\ & + \left[1-\exp\left(-\frac{\theta_{\mathrm{FoV},i}^2}{2m_i\sigma_{\mathrm{angle,u}}^2}\right)\right]\frac{\alpha_i\beta_i\zeta_i^2}{A_i h_i^{(l)}\Gamma(\alpha_i)\Gamma(\beta_i)} \\ & \times \underbrace{\int_0^{h_{\mathrm{th},i}} G_{1,3}^{3,0}\left[\frac{\alpha_i\beta_i}{A_i h_i^{(l)}}h_i \middle| \begin{matrix}\zeta_i^2 \\ \zeta_i^2-1, \alpha_i-1, \beta_i-1\end{matrix}\right]\mathrm{d}h_i}_{\triangleq I}. \end{aligned} \tag{B.1}$$

By (26) in [34], I in (B.1) can be further written as

$$I = h_{\mathrm{th},i}G_{2,4}^{3,1}\left[\frac{\alpha_i\beta_i}{A_i h_i^{(l)}}h_{\mathrm{th},i} \middle| \begin{matrix}0, \zeta_i^2 \\ \zeta_i^2-1, \alpha_i-1, \beta_i-1, -1\end{matrix}\right]. \tag{B.2}$$

Then, by (9.31.5) in [27], eq. (B.2) can be written as

$$I = \frac{A_i h_i^{(\mathrm{l})}}{\alpha_i \beta_i} G_{2,4}^{3,1}\left[\frac{\alpha_i \beta_i}{A_i h_i^{(\mathrm{l})}} h_{\mathrm{th},i} \,\middle|\, \begin{matrix} 1, \zeta_i^2 + 1 \\ \zeta_i^2, \alpha_i, \beta_i, 0 \end{matrix} \right]. \tag{B.3}$$

Submitting (B.3) and (18) into (B.1), we obtain (19).

APPENDIX C
PROOF OF *Theorem 3*

According to (18), when the transmit power P_{t} tends to infinity, we have

$$\lim_{P_{\mathrm{t}} \to \infty} \; h_{\mathrm{th},i} = \lim_{P_{\mathrm{t}} \to \infty} \; \sqrt{\frac{\Upsilon_{\mathrm{th}} \sigma_{\mathrm{n},i}^2}{2R^2 P_{\mathrm{t}}^2}} = 0. \tag{C.1}$$

In (19), the Meijer's G-function cannot provide intuitive insights on the behavior of $h_{\mathrm{th},i}$. For a large transmit power P_{t}, the outage probability is dominated by the behavior of the PDF near the origin. Therefore, by employing (07.34.06.0006.01) in [37] or [6], we can approximate (19) as

$$\begin{aligned} p_i \approx \exp\left(-\frac{\theta_{\mathrm{FoV},i}^2}{2 m_i \sigma_{\mathrm{angle,u}}^2} \right) + \left[1 - \exp\left(-\frac{\theta_{\mathrm{FoV},i}^2}{2 m_i \sigma_{\mathrm{angle,u}}^2} \right) \right] \\ \times \frac{\zeta_i^2 \Gamma(\alpha_i - \kappa_i) b_i}{\Gamma(\alpha_i) \Gamma(\beta_i) \kappa_i} \left(\frac{\alpha_i \beta_i}{A_i h_i^{(\mathrm{l})}} \right)^{\kappa_i} (h_{\mathrm{th},i})^{\kappa_i}, \\ \kappa_i = \min(\zeta_i^2, \beta_i), \end{aligned} \tag{C.2}$$

where $b_i = 1/(\zeta_i^2 - \beta_i)$ if $\zeta_i^2 > \beta_i$, and $b_i = \Gamma(\beta_i - \zeta_i^2)$ if $\zeta_i^2 < \beta_i$. Because the small-scale turbulence eddies parameter $\beta_i > 1$ [38], the inequality $\kappa_i > 1$ always holds.

By (C.1), the second term in (C.2) tends to zero when P_{t} tends to infinity. Therefore, *Theorem 3* holds.

REFERENCES

[1] Y. Ma, J.-Y. Wang, J.-B. Wang, M. Lin, H. Zhang, and C. Chang, "Outage performance analysis and parameter optimization of hovering UAV-based FSO system," in *Proc. IEEE Int. Conf. Commun. (ICC)*, Dublin, Ireland, Jun. 2020, pp. 1–6.

[2] A. S. Hamza, J. S. Deogun, and D. R. Alexander, "Classification framework for free space optical communication links and systems," *IEEE Commun. Surveys Tuts.*, vol. 21, no. 2, pp. 1346–1382, 2nd Quart., 2019.

[3] M. A. Khalighi and M. Uysal, "Survey on free space optical communication: A communication theory perspective," *IEEE Commun. Surveys Tuts.*, vol. 16, no. 4, pp. 2231–2258, 4th Quart., 2014.

[4] X. Li, X. Zhao, P. Zhang, and S. Tong, "BER performance of FSO communication system with differential signaling over correlated atmospheric turbulence fading," *China Commun.*, vol. 17, no. 4, pp. 51–65, Apr. 2020.

[5] J.-Y. Wang, J.-B. Wang, M. Chen, Y. Tang, and Y. Zhang, "Outage analysis for relay-aided free-space optical communications over turbulence channels with nonzero boresight pointing errors," *IEEE Photon. J.*, vol. 6, no. 4, pp. 1–15, Aug. 2014.

[6] S. Huang, V. Shah-Mansouri, and M. Safari, "Game-theoretic spectrum trading in RF relay-assisted free-space optical communications," *IEEE Trans. Wireless Commun.*, vol. 18, no. 10, pp. 4803–4815, Oct. 2019.

[7] W. Fawaz, C. Abou-Rjeily, and C. Assi, "UAV-aided cooperation for FSO communication systems," *IEEE Commun. Mag.*, vol. 56, no. 1, pp. 70–75, Jan. 2018.

[8] M. Alzenad, M. Z. Shakir, H. Yanikomeroglu, and M.-S. Alouini, "FSO-based vertical backhaul/fronthaul framework for 5G+ wireless networks," *IEEE Commun. Mag.*, vol. 56, no. 1, pp. 218–224, Jan. 2018.

[9] Y. Dong, M. Z. Hassan, J. Cheng, M. J. Hossain, and V. C. M. Leung, "An edge computing empowered radio access network with UAV-mounted FSO fronthaul and backhaul: Key challenges and approaches," *IEEE Wireless Commun.*, vol. 25, no. 3, pp. 154–160, Jun. 2018.

[10] Y. Zeng, Q. Wu, and R. Zhang, "Accessing from the sky: A tutorial on UAV communications for 5G and beyond," *Proc. IEEE*, vol. 107, no. 12, pp. 2327–2375, Dec. 2019.

[11] A. Kaadan, H. Refai, and P. Lopresti, "Spherical FSO receivers for UAV communication: Geometric coverage models," *IEEE Trans. Aerosp. Electron. Syst.*, vol. 52, no. 5, pp. 2157–2167, Oct. 2016.

[12] A. Kaadan, H. H. Refai, and P. G. LoPresti, "Multielement FSO transceivers alignment for inter-UAV communications," *J. Lightw. Technol.*, vol. 32, no. 24, pp. 4785–4795, Dec. 15, 2014.

[13] H. Ajam, M. Najafi, V. Jamali, and R. Schober, "Ergodic sum rate analysis of UAV-based relay networks with mixed RF-FSO channels," *IEEE Open J. Commun. Soc.*, vol. 1, pp. 164–178, Jan. 2020.

[14] J.-H. Lee, K.-H. Park, Y.-C. Ko, and M.-S. Alouini, "Throughput maximization of mixed FSO/RF UAV-aided mobile relaying with a buffer," *IEEE Trans. Wireless Commun.*, vol. 20, no. 1, pp. 683–694, Jan. 2021.

[15] M. Najafi, H. Ajam, V. Jamali, P. D. Diamantoulakis, G. K. Karagiannidis, and R. Schober, "Statistical modeling of the FSO fronthaul channel for UAV-based communications," *IEEE Trans. Commun.*, vol. 68, no. 6, pp. 3720–3736, Jun. 2020.

[16] S. Huang and M. Safari, "Free-space optical communication impaired by angular fluctuations," *IEEE Trans. Wireless Commun.*, vol. 16, no. 11, pp. 7475–7487, Nov. 2017.

[17] V. V. Mai and H. Kim, "Beam size optimization and adaptation for high-altitude airborne free-space optical communication systems," *IEEE Photon. J.*, vol. 11, no. 2, pp. 1–13, Apr. 2019.

[18] M. T. Dabiri, S. M. S. Sadough, and M. A. Khalighi, "Channel modeling and parameter optimization for hovering UAV-based free-space optical links," *IEEE J. Sel. Areas Commun.*, vol. 36, no. 9, pp. 2104–2113, Sep. 2018.

[19] M. T. Dabiri, M. Rezaee, I. S. Ansari, and V. Yazdanian, "Channel modeling for UAV-based optical wireless links with nonzero boresight pointing errors," *IEEE Trans. Veh. Technol.*, vol. 69, no. 12, pp. 14238–14246, Dec. 2020.

[20] A. A. Farid and S. Hranilovic, "Outage capacity optimization for free-space optical links with pointing errors," *J. Lightw. Technol.*, vol. 25, no. 7, pp. 1702–1710, Jul. 2007.

[21] M. A. Amirabadi and V. T. Vakili, "A new optimization problem in FSO communication system," *IEEE Commun. Lett.*, vol. 22, no. 7, pp. 1442–1445, Jul. 2018.

[22] J.-H. Lee, K.-H. Park, M.-S. Alouini, and Y.-C. Ko, "Free space optical communication on UAV-assisted backhaul networks: Optimization for service time," in *Proc. IEEE Globecom Workshops (GC Wkshps)*, Waikoloa, HI, USA, Dec. 2019, pp. 1–6.

[23] D. Wu, X. Sun, and N. Ansari, "An FSO-based drone assisted mobile access network for emergency communications," *IEEE Trans. Netw. Sci. Eng.*, vol. 7, no. 3, pp. 1597–1606, Jul. 2020.

[24] O. Esrafilian, R. Gangula, and D. Gesbert, "Learning to communicate in UAV-aided wireless networks: Map-based approaches," *IEEE Internet Things J.*, vol. 6, no. 2, pp. 1791–1802, Apr. 2019.

[25] B. Zhu, J. Cheng, M.-S. Alouini, and L. Wu, "Relay placement for FSO multihop DF systems with link obstacles and infeasible regions," *IEEE Trans. Wireless Commun.*, vol. 14, no. 9, pp. 5240–5250, Sep. 2015.

[26] M. T. Dabiri and S. M. S. Sadough, "Optimal placement of UAV-assisted free-space optical communication systems with DF relaying," *IEEE Commun. Lett.*, vol. 24, no. 1, pp. 155–158, Jan. 2020.

[27] I. S. Gradshteyn and I. M. Ryzhik, *Table of Integrals, Series, and Products*, 7th ed. New York, NY, USA: Academic, 2007.

[28] L. C. Andrews and R. L. Phillips, *Laser Beam Propagation Through Random Media*, vol. 52. Bellingham, WA, USA: SPIE, 2005.

[29] T. V. Pham, T. C. Thang, and A. T. Pham, "Average achievable rate of spatial diversity MIMO-FSO over correlated gamma–gamma fading channels," *IEEE/OSA J. Opt. Commun. Netw.*, vol. 10, no. 8, pp. 662–674, Aug. 2018.

[30] R. Boluda-Ruiz, A. García-Zambrana, C. Castillo-Vázquez, and B. Castillo-Vázquez, "Novel approximation of misalignment fading modeled by Beckmann distribution on free-space optical links," *Opt. Exp.*, vol. 24, no. 20, pp. 22635–22649, Oct. 2016.

[31] R. Gagliardi and S. Karp, *Optical Communications*. Hoboken, NJ, USA: Wiley, 1995.

[32] M. T. Dabiri, S. M. S. Sadough, and I. S. Ansari, "Tractable optical channel modeling between UAVs," *IEEE Trans. Veh. Technol.*, vol. 68, no. 12, pp. 11543–11550, Dec. 2019.

[33] F. Yang, J. Cheng, and T. A. Tsiftsis, "Free-space optical communication with nonzero boresight pointing errors," *IEEE Trans. Commun.*, vol. 62, no. 2, pp. 713–725, Feb. 2014.

[34] V. S. Adamchik and O. I. Marichev, "The algorithm for calculating integrals of hypergeometric type functions and its realization in REDUCE system," in *Proc. Int. Symp. Symbolic Algebr. Comput. (ISSAC)*, Tokyo, Japan, 1990, pp. 212–224.
[35] M. Sheng, P. Jiang, Q. Hu, Q. Su, and X.-X. Xie, "End-to-end average BER analysis for multihop free-space optical communications with pointing errors," *J. Opt.*, vol. 15, no. 5, pp. 1–7, Apr. 2013.
[36] S. C. Gupta, "Delta function," *IEEE Trans. Educ.*, vol. E-7, no. 1, pp. 16–22, Mar. 1964.
[37] Wolfram. *The Wolfram Functions Site*. Accessed: Jun. 20, 2021. [Online]. Available: http://functions.wolfram.com/
[38] N. Wang and J. Cheng, "Moment-based estimation for the shape parameters of the gamma-gamma atmospheric turbulence model," *Opt. Exp.*, vol. 18, no. 12, pp. 12824–12831, Jun. 2010.

Jin-Yuan Wang (Member, IEEE) received the B.S. degree in communication engineering from the Shandong University of Science and Technology, Qingdao, China, in 2009, the M.S. degree in electronic and communication engineering from the Nanjing University of Aeronautics and Astronautics, Nanjing, China, in 2012, and the Ph.D. degree in information and communication engineering from Southeast University, Nanjing, in 2015. From January 2016 to June 2019, he was a Lecturer with the Nanjing University of Posts and Telecommunications, Nanjing. Since July 2019, he has been an Associate Professor with the Nanjing University of Posts and Telecommunications. He has authored or coauthored over 100 journal articles/conference papers. His current research interest includes visible light communications. He serves as the Workshop Chair for ICFEICT 2021. He serves as a Technical Program Committee Member for many international conferences, such as IEEE ICC and WTS. He also serves as a reviewer for many journals.

Yang Ma received the B.S. degree in integrated circuit design and integrated systems from Hangzhou Dianzi University, Hangzhou, China, in 2018, and the M.S. degree in communication and information systems from the National Mobile Communications Research Laboratory, Southeast University, Nanjing, China, in 2021. His current research interests include wireless optical communications and unmanned aerial vehicle communications.

Rong-Rong Lu received the B.S. degree in electronic science and technology from the Nanjing University of Posts and Telecommunications, Nanjing, China, in 2019, where she is currently pursuing the M.S. degree in communication and information systems. Her current research interest includes optical wireless communications.

Jun-Bo Wang (Member, IEEE) received the B.S. degree in computer science from the Hefei University of Technology, Hefei, China, in 2003, and the Ph.D. degree in communications engineering from the National Mobile Communications Research Laboratory, Southeast University, Nanjing, China, in 2008. He is currently an Associate Professor with the National Mobile Communications Research Laboratory, Southeast University. From October 2008 to August 2013, he was with the Nanjing University of Aeronautics and Astronautics, China. From March 2011 to February 2013, he was a Post-Doctoral Fellow with the National Laboratory for Information Science and Technology, Tsinghua University, Beijing, China. From September 2016 to September 2018, he held the European Commission Marie Skłodowska-Curie Fellowship. He was a Research Fellow with the University of Kent, U.K. His current research interests include visible light communications, information theory, and coding.

Min Lin (Member, IEEE) received the B.S. degree in electrical engineering from the National University of Defense Technology, Changsha, China, in 1993, the M.S. degree in electrical engineering from the Nanjing Institute of Communication Engineering, Nanjing, China, in 2000, and the Ph.D. degree in electrical engineering from Southeast University, Nanjing, in 2008. From April 2015 to October 2015, he has visited the University of California, Irvine, as a Senior Research Fellow. He is currently a Professor and a Supervisor of Ph.D. and graduate students with the Nanjing University of Posts and Telecommunications, Nanjing, China. He has authored or coauthored over 130 articles. His current research interests include wireless communications and array signal processing. He has served as the Track Chair for Satellite and Space Communications (SSC) of IEEE ICC 2019 and a TPC Member for many IEEE sponsored conferences, such as IEEE ICC and GLOBECOM.

Julian Cheng (Senior Member, IEEE) received the B.Eng. degree (Hons.) in electrical engineering from the University of Victoria, Victoria, BC, Canada, in 1995, the M.Sc. (Eng.) degree in mathematics and engineering from Queens University, Kingston, ON, Canada, in 1997, and the Ph.D. degree in electrical engineering from the University of Alberta, Edmonton, AB, Canada, in 2003. He is currently a Full Professor with the School of Engineering, Faculty of Applied Science, The University of British Columbia, Kelowna, BC, Canada. He was with Bell Northern Research and NORTEL Networks. His current research interests include machine learning and deep learning for wireless communications, optical wireless technology, and quantum communications. He was the Co-Chair of the 12th Canadian Workshop on Information Theory in 2011, the 28th Biennial Symposium on Communications in 2016, and the Sixth EAI International Conference on Game Theory for Networks in 2016. He currently serves as an Area Editor for the IEEE TRANSACTIONS ON COMMUNICATIONS. He was a past Associate Editor of the IEEE TRANSACTIONS ON COMMUNICATIONS, the IEEE TRANSACTIONS ON WIRELESS COMMUNICATIONS, the IEEE COMMUNICATIONS LETTERS, and IEEE ACCESS. He served as a Guest Editor for a Special Issue of the IEEE JOURNAL ON SELECTED AREAS IN COMMUNICATIONS on Optical Wireless Communications. He is also a Registered Professional Engineer with the Province of British Columbia, Canada. He serves as the President for the Canadian Society of Information Theory and the Secretary for the Radio Communications Technical Committee of IEEE Communications Society.